Whispering-gallery mode resonators for highly unidirectional laser action

Qi Jie Wang[a,1,2], Changling Yan[a,1,3], Nanfang Yu[a], Julia Unterhinninghofen[b], Jan Wiersig[b], Christian Pflügl[a], Laurent Diehl[a], Tadataka Edamura[c], Masamichi Yamanishi[c], Hirofumi Kan[c], and Federico Capasso[a,4]

[a]School of Engineering and Applied Sciences, Harvard University, 9 Oxford Street, Cambridge, MA 02138; [b]Institut für Theoretische Physik, Universität Magdeburg, Postfach 4120, D-39016 Magdeburg, Germany; and [c]Central Research Laboratory, Hamamatsu Photonics K.K., Hamamatsu 434-8601, Japan

Contributed by Federico Capasso, October 21, 2010 (sent for review August 1, 2010)

Optical microcavities can be designed to take advantage of total internal reflection, which results in resonators supporting whispering-gallery modes (WGMs) with a high-quality factor (Q factor). One of the crucial problems of these devices for practical applications such as designing microcavity lasers, however, is that their emission is nondirectional due to their radial symmetry, in addition to their inefficient power output coupling. Here we report the design of elliptical resonators with a wavelength-size notch at the boundary, which support in-plane highly unidirectional laser emission from WGMs. The notch acts as a small scatterer such that the Q factor of the WGMs is still very high. Using midinfrared ($\lambda \sim 10\ \mu$m) injection quantum cascade lasers as a model system, an in-plane beam divergence as small as 6 deg with a peak optical power of ∼5 mW at room temperature has been demonstrated. The beam divergence is insensitive to the pumping current and to the notch geometry, demonstrating the robustness of this resonator design. The latter is scalable to the visible and the near infrared, thus opening the door to very low-threshold, highly unidirectional microcavity diode lasers.

Following the first description of the whispering-gallery mode (WGM) phenomenon in the acoustic regime by Lord Rayleigh in London's St Paul's Cathedral (1) and its subsequent analysis in terms of guided surface waves by Raman and Sutherland (2), its study was later extended to the radiofrequency (3) and optical domains (4) through the investigation of the ionosphere and solid spheres, respectively. WGMs were later investigated in liquid droplets (5) and microdisk diode lasers (6), opening a previously undescribed direction in photonics technology. WGM resonators offer great promise for investigation in the physical sciences (6–8), and applications of these devices have spanned a wide range from unique laser sources (9) and dynamic filters in communications (10) to sensors (11). One drawback, however, is that, in rotationally symmetric cavities (6, 12), WGMs can only be coupled out inefficiently and isotropically through scattering of evanescent waves by surface roughness or diffraction losses when the radius of curvature is comparable to the wavelength (9).

Previously, this problem was addressed through evanescent coupling using prisms (13), in-plane waveguide (14), or tapered fibers (15). The technique of using tapered waveguide (16) for coupling high Q WGMs out of cavities is quite successful for the study of fundamental cavity physics; however, it requires careful alignment and the devices are relatively sensitive to mechanical vibrations or other variations in the surrounding environment, which limit its usage for practical applications such as achieving microcavity lasers with directional emission. Another approach is to break the rotational symmetry by using deformed optical microcavities to increase the directionality of emission and power collection efficiency (17, 18), which has the advantage of easy and robust fabrication. The most successful designs include quadrupolar shaped lasers (19, 20) and spiral-shaped lasers (21, 22). However, all deformed microcavities studied in the literature have the problem that the Q factor degrades significantly as the deformation increases (23); in most of the cases WGMs are no longer supported in the cavity. Recently, a Limaçon-shaped microcavity (24) was proposed to improve directionality and was soon demonstrated experimentally in the midinfrared (25, 26) and near-infrared spectral regions (27, 28). The far-field divergence angle of the main lobe of these devices, however, is about 30 or more degrees and side lobes persist. Here, we demonstrate highly unidirectional laser action, with FWHM beam divergence angle of ∼6 deg, from WGMs in elliptical-shaped quantum cascade laser (QCL) microcavities with a wavelength-size notch at the boundary. For resonator aspect ratios near the optimum for low beam divergence, the latter is insensitive to variations in notch size and in pumping current, proving the robustness of the design.

Results and Discussion

We chose an elliptical resonator because it possesses WGMs with very high Q factors (29) for shapes with various long-to-short aspect ratio Y/X. A notch of size comparable to the wavelength in the material, suitably defined on the boundary, will diffract light toward the opposite boundary. Fig. 1*A* illustrates how the aspect ratio Y/X of the elliptical resonator (blue curve) was optimized to achieve maximum collimation. The notch is located at the intersection of the short axis and the boundary (point O). In order to achieve collimation of the majority of the light scattered by the notch, we exploit a well-known property of the ellipse: For any given refractive index $n > 1$, one can find an ellipse (auxiliary ellipse) such that all incoming parallel rays are collected into one of its foci (30); conversely in the reciprocal process light emerging from the left focus of the auxiliary ellipsis in Fig. 1*A* is refracted by its *right half-side* into parallel rays. Note that the notch is located at one of the foci of the auxiliary ellipse (red dashed curve), but not at the focus of the elliptical resonator. The Y/X ratio of the elliptical resonator is now chosen such that its boundary best (i.e., over the largest possible angle 2θ) approximates that of the auxiliary ellipse.

In quantitative terms, let $r(\theta)$ be the distance between some point on the resonator boundary and point O, and $R(\theta)$ the distance between a corresponding point on the auxiliary ellipse and point O. Maximizing the range of angles θ where $R(\theta)$-$r(\theta)$ is negligible (here we set $|R(\theta)\text{-}r(\theta)|/R(\theta) \approx 1\%$ corresponding to the accuracy of fabrication), we find $\varepsilon \equiv Y/X$ is ∼1.2 for a refractive index $n_{\text{eff}} = 3.2$ for the laser material we used in the experiment

Author contributions: Q.J.W., C.Y., and N.Y. designed research; Q.J.W., C.Y., N.Y., J.U., J.W., C.P., L.D., T.E., M.Y., and H.K. performed research; Q.J.W., C.Y., N.Y., J.U., J.W., C.P., L.D., and F.C. analyzed data; and Q.J.W., C.Y., N.Y., J.U., J.W., and F.C. wrote the paper.

The authors declare no conflict of interest.

[1]Q.J.W. and C.Y. contributed equally to this work.

[2]Present address: School of Electrical and Electronic Engineering and School Physical and Mathematical Sciences, Nanyang Technological University, 50 Nanyang Avenue, 639798 Singapore.

[3]Present address: Changchun University of Science and Technology, Changchun, 130022, China.

[4]To whom correspondence should be addressed. E-mail: capasso@seas.harvard.edu.

This article contains supporting information online at www.pnas.org/lookup/suppl/doi:10.1073/pnas.1015386107/-/DCSupplemental.

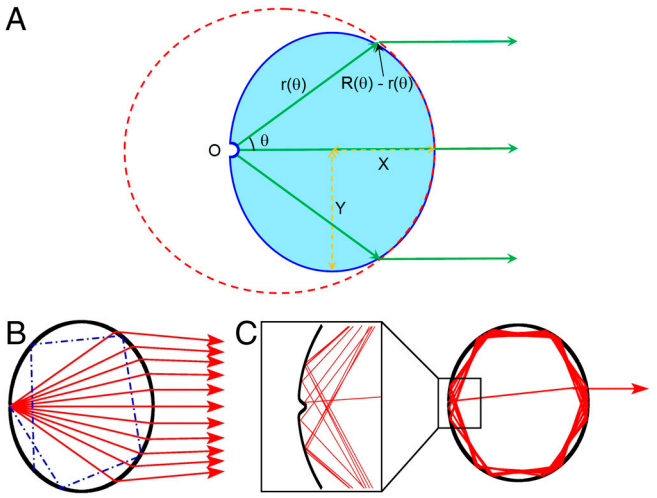

Fig. 1. Design principle of notched-elliptical resonator and simulated ray dynamics. (*A*) Schematic illustration of the notched-elliptical resonator. The green arrows indicate that light waves are scattered by the notch at point O, then collimated as a parallel beam in the far-field by the right-hand-side boundary of the notched ellipse. We utilize the well known focusing property of the ellipse (auxiliary ellipse in red) to achieve optimal collimation: The boundary of the notched-elliptical resonator (blue curve) is designed to best approximate that of the auxiliary ellipse within the largest possible range of $2\theta_{max}(\sim 70$ deg). The notch of the resonator is located at one of the foci of the auxiliary ellipse (red dashed curve). The optimal Y/X ratio is 1.2 for $n_{eff} = 3.2$. (*B*) Ray simulation of the collimation effect: a number of rays are started at the position of the notch with different outgoing angles, simulating a scattering process. They travel inside the cavity until they hit its boundary, upon which they either are specularly reflected or, if the angle of incidence at the surface is smaller than the critical angle for total internal reflection, get refracted out. The red, solid rays, which leave the notch under relatively smaller outgoing angles, get collimated; the collimation is worse for higher outgoing angles (outermost red rays). The blue dash-dotted ray leaves the notch at a high outgoing angle and is relaunched into a whispering-gallery mode. (*C*) Ray simulation of whispering-gallery mode dynamics. A single ray is started at some position along the resonator boundary with an initial condition such that the angle of incidence is larger than the critical angle. It is then specularly reflected many times, corresponding to a whispering-gallery-like mode, until at some point it hits the notch. It then gets reflected to the opposite boundary, is refracted out, and leaves the cavity parallel to the x axis due to the collimation effect. A magnification of the dynamics near the notch is shown.

(see *Materials and Methods*). This optimal value $\varepsilon = 1.2$ yields $2\theta_{max} = 70$ deg; thus indeed the majority of the light is collimated by the elliptical resonator. It is also possible to derive an analytical expression in the paraxial ray approximation for the optimal ε by starting rays at the notch, using Snell's law to find the far-field rays, and requiring that they are parallel. We find $\varepsilon = (2\text{-}2/n_{eff})^{1/2} \approx 1.17$ for $n_{eff} = 3.2$, which agrees well with the numerical result of 1.2.

We first employed ray simulations to analyze the proposed resonator. Fig. 1*B* demonstrates the collimation effect of many rays scattered by the notch. Fig. 1*C* shows that a single ray travels inside the resonator and is reflected many times by the resonator boundary, corresponding to a high Q factor WGM, until it hits the notch and escapes from the cavity at the opposite boundary.

We then calculated the optical modes in the cavity through wave simulations (see *Materials and Methods*). Fig. 2*A* shows the intensity distribution of the first-radial-order WGM, which is a transverse magnetic (TM) mode, as QCLs are TM polarized due to the intersubband transition selection rule (31), for a structure with $\varepsilon = 1.2$ and an optimized, in terms of minimum beam divergence, notch size $o = 3$ μm and $d = 2$ μm, where o and d refer to the width and the depth of the notch, respectively; see Fig. 3*B*. A Q factor as high as 590,000 is calculated for this mode without considering the material optical losses, which are dominated at the midinfrared wavelengths of QCLs by free carrier absorption (32). Inclusion of such losses in the simulation, as discussed later in the paper, leads to a much reduced Q factor. Fig. 2*B* shows the near-field intensity distribution outside the cavity of this mode. To show the details of the light scattered by the notch inside the cavity, we plot the light intensity distribution in a logarithmic scale; see Fig. 2*C*. Only the outermost part of this mode has an overlap with the notch, thus giving a high Q factor. Light is scattered by the notch to the right-hand-side boundary of the resonator (Fig. 2*C*). The refracted beams propagate almost parallel to the $\theta = 0$ direction, resulting in unidirectional emission (Fig. 2*D*). The weak backward refracted laser beams near position a in Fig. 2*B* are owning to the low transmission of light

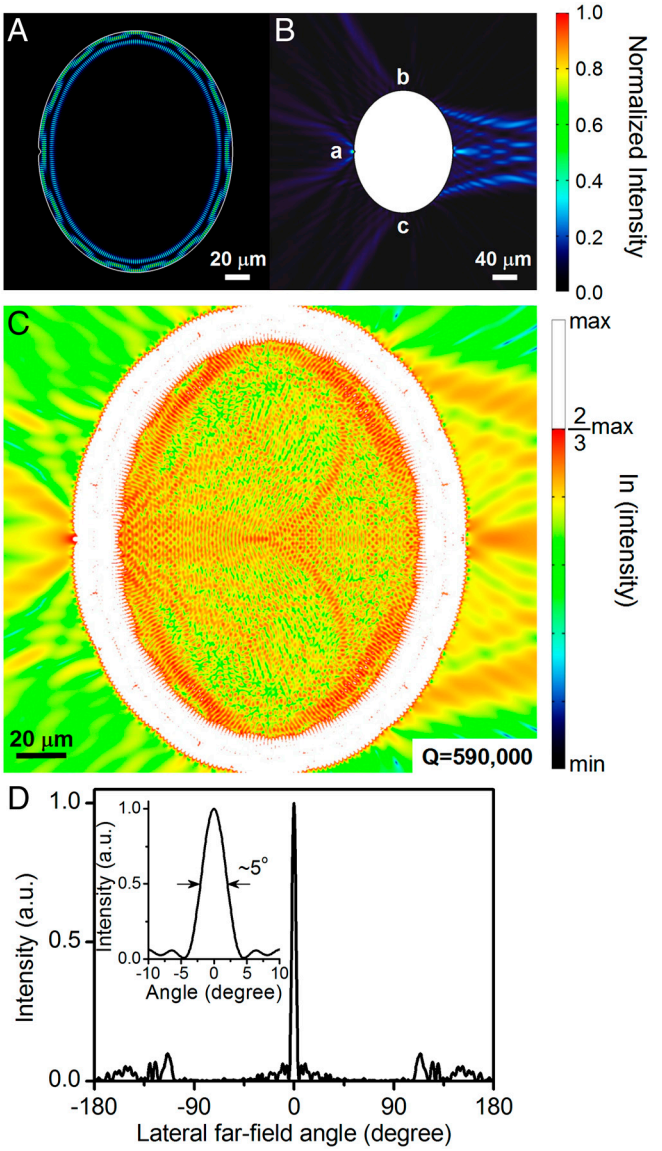

Fig. 2. Mode distribution by wave simulations. (*A*) Calculated mode intensity distribution of a device with $X = 80$ μm and $Y = 96$ μm and an optimized notch $o = 3$ μm and $d = 2$ μm in linear scale. The free-space wavelength is $\lambda = 10$ μm, and $\lambda_{eff} \sim 3.1$ μm is the wavelength in material. Shown is the first-radial-order WGM with even parity (see *SI Text*) with respect to the short axis of the resonator. (*B*) External near-field intensity distribution of the mode shown in *A*. The majority of the output power is collimated along the $\theta = 0$ direction. (*C*) The same mode intensity distribution of the mode in *A* plotted in a logarithmic scale. (*D*) Simulated far-field intensity distribution showing an in-plane beam divergence angle as narrow as ~5°. (*Inset*) The zoom-in plot of the far-field intensity profile.

out of the cavity through the notch. The two weak side peaks at positions b and c in Fig. 2*B* (corresponding to the two far-field peaks near ±120 deg in Fig. 2*D*), respectively, originate from a certain amount of light reflected toward b and c from different directions than from the notch, similar to the origin of the side peaks in TM Limaçon microcavity (see figure 3 in ref. 24 for elaboration). Higher-radial-order, lower Q factor, WG-like modes are also present (*SI Text*). Although the proposed scheme is demonstrated in a regime where the ratio of cavity size to wavelength in material $X/\lambda_{\text{eff}} \sim 26$ is relatively high, simulations show that the smallest notched-elliptical resonators with directional emission correspond to $X/\lambda_{\text{eff}} \sim 3$.

Simulations (*SI Text*) demonstrate that the far-field profile of transverse electric (TE) polarized modes is also highly directional, implying that the proposed concept is broadly applicable also to diode lasers operating in the near infrared and visible. The Q factor of the whispering-gallery modes is still very high in these structures for the same wavelength-to-size ratio. At relatively short wavelengths, e.g., $\lambda \sim 1$ μm, free carrier absorption is negligible and optical losses are small (33) (~0.5 cm^{-1}), limited by sidewall roughness of the cavity, and material absorption. This will lead to a much smaller Q-factor degradation than that at mid-IR wavelengths (optical loss is ~15.6 cm^{-1} for our QCLs). Thus we expect notched-elliptical resonators to be excellent for low-threshold, highly directional microcavity diode lasers. In support of this also note that for the same high Q ($\sim 1 \times 10^6$) Limaçon-shaped microcavity design (24), a Q factor of $\sim 2 \times 10^4$ was experimentally obtained for diode lasers emitting at $\lambda \sim 1$ μm (28) as compared to ~1,000 of mid-IR QCLs (26).

Note that an optical mode with a calculated very high Q factor of $>5 \times 10^6$ does exist in the cavity (*SI Text*). It resembles the mode in Figs. 2 *A–C* but with odd parity with respect to the short axis of the notched-elliptical resonator. However, due to its strongly reduced overlap with the notch, it has a much smaller output coupling than the even parity mode of Figs. 2 *A–C*. In addition, due to the existence of unavoidable material optical losses, both odd and even parity modes start to lase at almost the same pumping current in experiments. Therefore, the odd parity mode is not observed in the far-field profile measurement but is visible in the measured spectra (as seen in Fig. 3*D*) because the spectrometer helps discriminate this weak signal from the background at low pumping currents.

Devices with different dimensions and notch sizes were fabricated and tested in pulsed mode operation at room temperature (*Materials and Methods*). Fig. 3 *A* and *B* show, respectively, scanning electron microscope (SEM) images of a representative device and its vertical sidewall. Fig. 3*C* presents the light output power versus current (L-I) characteristics of this device. The measured Q factor of our devices is ~1,260, deduced from threshold current density and the gain coefficient measurements (32), which agrees well with the simulation value when the relatively high optical losses at the midinfrared wavelengths (32) (~15.6 cm^{-1} for our devices, deduced from the measurements of threshold current densities versus cavity lengths of ridge laser devices) are included in the simulation. Thus for the QCL case, the threshold current density and Q factor of the notched-elliptical lasers are similar to those of Limaçon-shaped QCLs (25, 26), respectively, due to the high optical losses.

Fig. 3*D* presents the emission spectra of the notched-elliptical QCLs measured at different pumping currents. The laser operates in single mode at $\lambda \sim 10$ μm near the threshold current (520 mA), corresponding to the mode with the highest Q factor ($>5 \times 10^6$) with odd parity. At a pumping current of 750 mA, two sets of optical modes appear, indicated by blue and red arrows, corresponding respectively to the first two highest Q factor WGMs with even and odd parities. The average mode spacing of each set is approximately 5.80 cm^{-1}, which agrees very well with the calculated value of 5.85 cm^{-1} for both odd parity and even parity modes. At a higher pumping current several additional modes appear, indicated by green arrows, corresponding to lower Q factor type of modes as the one described in the *SI Text* (Fig. S1*A*).

The schematic and the 2D far field of the device are displayed in Fig. 4 *A* and *B*, respectively. A much narrower beam divergence angle of 6 deg in the plane of the laser cavity than previously reported in microcavity (26) and Fabry–Perot ridge QC lasers is demonstrated. As the vertical far-field emission distribution (due to diffraction at the small light-emitting aperture in the vertical direction of the resonator) does not affect the characteristics of WGM in the plane of the resonator, such as the mode intensity

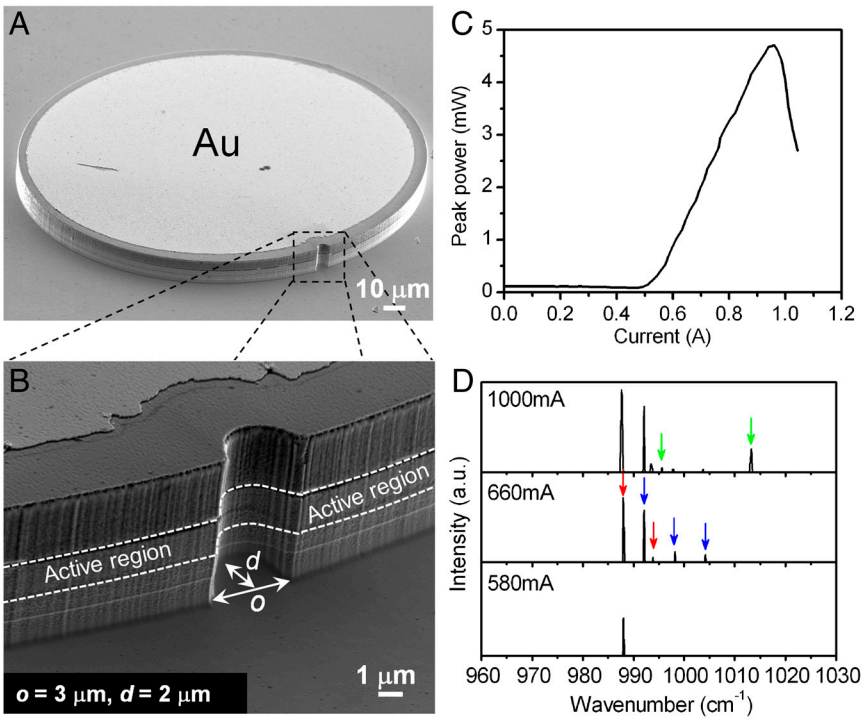

Fig. 3. Fabricated device and its electrical and optical characteristics. (*A*) Scanning electron microscope image of the notched-elliptical resonator with a minor radius $X = 80$ μm, a major radius $Y = 96$ μm, and notch dimensions $o = 3$ μm, and $d = 2$ μm. The top gold contact is deposited for electric pumping. (*B*) Zoom-in view of the device showing the smooth sidewall of the laser cavity. The two white lines indicate the boundaries of the active region. (*C*) Room temperature L-I characteristics of the device measured in pulsed mode operation with a duty cycle of 1%. A peak output power of ~5 mW, a threshold current density ~2.0 kA/cm^2, and a slope efficiency of ~11 mW/A were obtained. (*D*) The laser spectra of the device at different pumping currents. The threshold current of the laser is around 520 mA. At a pumping current of 750 mA, two sets of WGMs, indicated by the blue and red arrows, are present; at an even higher pumping current (1,000 mA), several additional modes appear, indicated by green arrows, corresponding to lower Q-factor modes.

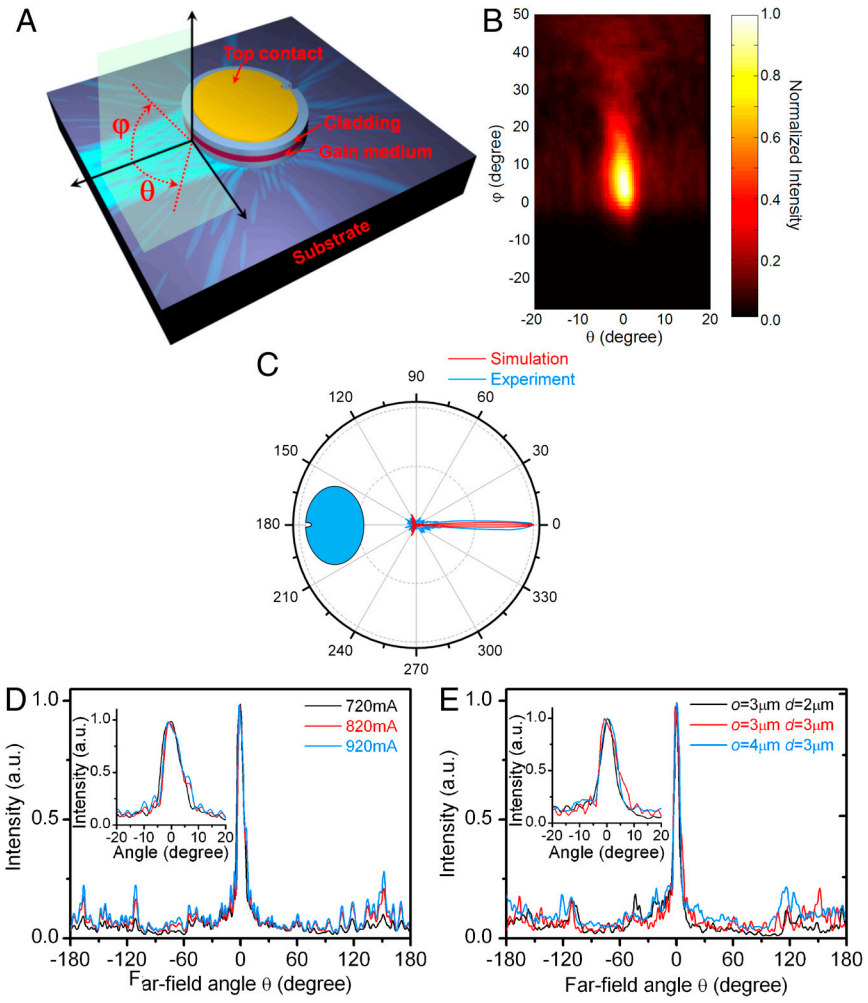

Fig. 4. Far-field profiles of different microcavity lasers. (*A*) Schematic of the device. (*B*) Measured two-dimensional far-field intensity distributions of a representative device with a minor radius $X = 80$ μm, a major radius $Y = 96$ μm, and a notch dimension $o = 3$ μm, $d = 2$ μm at a pumping current of ~720 mA. (*C*) The experimental (blue line) and simulated (red line) in-plane far-field intensity profiles in polar coordinate for the device in *B*. The measurements were taken at a current of 720 mA. The small discrepancy between the wave simulation and the measured data is most likely due to the surface roughness that broadens the main lobe of the emission. The far-field profiles are normalized to their maximum values. The simulated far-field profiles of two high Q-factor modes with even and odd parities were included because at the above pumping current both modes exist in the cavity. As the power out-coupling of the even parity mode is much higher than that of the odd parity mode (*SI Text*), the overall far-field intensity profile is dominated by the mode with even parity. (*D*) Measured far-field profiles of the device in *B* at different pumping currents of 720 mA, 820 mA, and 920 mA, respectively. (*Inset*) The zoom-in plot of the far-field profiles from −20 deg to +20 deg. (*E*) Comparison of the measured far-field profiles for devices with slightly different notch sizes near the optimum $o = 3$ μm, $d = 2$ μm. (*Insets*) Zoom-in plots of the far-field profiles.

distribution in the resonator and the lateral far-field behavior, the employed 2D simulation method can well explain the measured 2D far-field profile. Thus, good agreement is observed between the experimental and simulated far-field intensity profiles (Fig. 4*C*). The measured vertical far-field divergence angle is about 20 deg. Further reduction of vertical beam divergence could be achieved by patterning integrated plasmonic collimators (34) on the sidewall of the cavity through soft lithographic techniques (35), which makes possible patterning arbitrary nanoscale metallic features onto nonplanar surfaces. All the far-field profiles are essentially the same at different pumping currents from 720 mA to 920 mA (Fig. 4*D*). The far-field profiles (Fig. 4*E*) are insensitive to variations of the notch sizes from 2 μm to 4 μm, a deviation well within fabrication uncertainties. We note that ref. 36 also briefly discussed numerical simulations of a notched ellipse but for the situation of microcavities with dimensions comparable to the free-space wavelength and that the lens effect of the ellipse was not discussed. A "point scatterer" (37) in circular shaped microresonators has also been proposed recently to achieve directional emission. However, the shape of the resonator is not optimized and the structure is difficult to fabricate as the "high-index scatterer" is placed inside the cavity.

Fig. 5*A* shows the calculated directionality, defined as FWHM divergence angle, and the optical output power emitted into ±20 deg as a function of ε with the notch size/shape kept unchanged. The measured peak output power and the slope efficiency are plotted in Fig. 5*B* as a function of ε. Fig. 5*C* shows the measured far-field intensity profiles at different ε for $X = 80$ μm, $o = 3$ μm, and $d = 2$ μm. These calculations show that ε can be used as a design parameter to control the far-field profile. Beam profiles can also be manipulated by changing the notch size significantly (*SI Text*).

In summary, we have demonstrated highly unidirectional light emission from WGM lasers with in-plane beam divergence as small as 6 deg. The insensitivity of the device divergence to different notch sizes and to drive currents demonstrates the robustness of this type of resonator. To increase the output power of the device, one can choose to increase ε moderately (Fig. 5*B*) or change the notch size to scatter more power out of the cavity. Because our preliminary simulations show that the notched-elliptical resonator efficiently collimates also TE polarized modes that are typical for diode lasers this new resonator can also be used to achieve highly unidirectional near-infrared and visible WGM lasers. Furthermore, the successful realization of these simple-structured microcavity devices through standard photolithographic fabrication makes small-volume directional light sources possible for many important applications in, e.g., photonic integrated circuits, optical communications, and medical/biological high-sensitive sensors (8). It also allows an easy approach for studying microcavity physics (38) by coupling out light directly from the microcavities without external waveguides. We believe that the promising characteristics of notched-elliptical resonators, e.g., high Q factor, high directionality, robust fabrication, and wafer-based geometry, will lead to a previously undescribed phase of research and development on optical microcavities, where problems such as high-density chip-scale integration of collimated light sources in a lab-on-a-chip environment could be addressed.

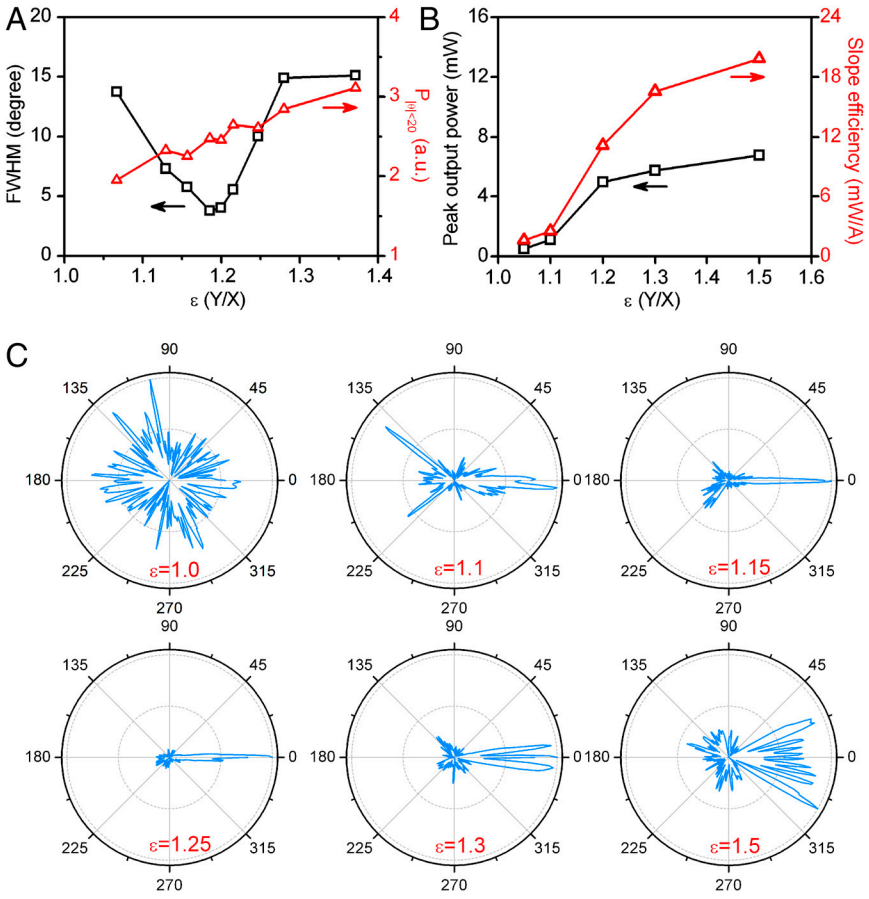

Fig. 5. Sensitivity of collimation. (*A*) Wave simulations of the directionality in terms of the FWHM and the optical output power within ±20 deg $P_{|\theta|<20}$ versus ε of the devices for $X = 80$ μm, $o = 3$ μm, and $d = 2$ μm. When $\varepsilon = 1.2$, the notched ellipse gives the best directionality while maintaining significant output power. The increase of the latter with larger ε is due to the fact that the effective lens aperture (right-hand-side boundary of the resonator) increases, collecting more light scattered from the notch. Simultaneously, the directionality of the far-field profile does not significantly increase for ε from 1.1 to 1.3. (*B*) Measured peak optical power and slope efficiency as a function of ε from various devices with the same $X = 80$ μm. The output power was collected with a power meter placed along the $\theta = 0$ direction with a collection angle of 100 deg. As expected, both the output power and the slope efficiency increase with increasing ε. (*C*) Experimental results of the far-field intensity profiles with ε in the range from 1.0 to 1.5.

Materials and Methods

Device Fabrication. We fabricated QCLs with different cavity sizes $X = 50$, 80, and 110 μm, and different axis ratio $\varepsilon = 1.0$, 1.1, 1.15, 1.2, 1.25, 1.3, and 1.5. The QCL material is the same as the one used in ref. 26 designed at an emission wavelength $\lambda \sim 10$ μm. Devices with different notch sizes near the optimum and significantly away from the optimum were fabricated. Standard photolithography was used to define the contour of the laser cavity, shown in Fig. 3*A*, and the structure was etched through the gain medium using inductively coupled plasma reactive ion etching to obtain vertical and smooth sidewalls. Then, the top and back metal contacts (Ti/Au: 10 nm/200 nm) were deposited. A SEM image of the device sidewall (Fig. 3*B*) shows a roughness of about 300 nm, which gives minor scattering in the midinfrared wavelength range.

Simulations. Wave simulations for the cavities without considering gain were carried out by solving Maxwell's equations numerically using the boundary element method (24). Our simulations show that the shape of the notch does not play a significant role; therefore, a Gaussian shape was chosen as it is numerically convenient. In the simulations, the equation used to describe the boundary of the notched-elliptical resonator is $x = \{1/\varepsilon - \delta \exp[-0.5(\varphi - \pi)^2/(0.25\Theta^2)]\cos(\phi)\}$ and $y = \sin(\phi)$ in polar coordinates, where ϕ is the polar angle to the center of the notched ellipse; $\varepsilon = Y/X$; $X = 80$ μm; δ and Θ determine the depth d and width o of the notch. An effective refractive index $n_{\text{eff}} \approx 3.2$ for TM polarization is used in the simulations for $\lambda = 10$ μm (λ is the wavelength in free space), deduced from the measurement of the mode spacing of a Fabry–Perot-type ridge QCL fabricated from the same material that is used for the notched-elliptical resonators.

Measurements. The processed devices were electric pumped and tested in pulsed mode at room temperature with 125-ns current pulses at 80-kHz repetition rate. The far-field profiles of our devices were measured using a setup described in ref. 34. The tested device was mounted at the center of a motorized rotation stage with 0.5° resolution, and a midinfrared mercury–cadmium–telluride detector positioned 10 cm away from the devices was scanned to measure the output of the laser. Power measurements were carried out with a calibrated power meter. Devices with a smaller size of $X = 50$ μm exhibited continuous wave operation above cryogenic temperature (*SI Text*).

ACKNOWLEDGMENTS. The authors gratefully acknowledge fruitful discussions with Martina Hentschel. Margherita Maiuri helped measure the far-field profiles of some devices. Device fabrication was carried out at the Center for Nanoscale Systems at Harvard University, a member of the National Nanotechnology Infrastructure Network. The Harvard authors acknowledge financial support from the Air Force Office of Scientific Research. Financial support from the Deutsche Forschungsgemeinschaft research group 760 is gratefully acknowledged by J.U. and J.W.

1. Rayleigh L (1912) The problem of the whispering gallery. *Scientific Papers*, (Cambridge University, Cambridge, England), 5, pp 617–620.
2. Raman CV, Sutherland GA (1921) Whispering-gallery phenomena at St. Paul's Cathedral. *Nature* 108:42.
3. Budden KG, Martin HG (1962) The ionosphere as a whispering gallery. *P Roy Soc Lond A Mat* 265:554–569.
4. Garrett CGB, Kaiser W, Bond WL (1961) Stimulated emission into optical whispering gallery modes of spheres. *Phys Rev* 124:1807–1809.
5. Qian SX, Snow JB, Tzeng HM, Chang RK (1986) Lasing droplets—highlighting the liquid-air interface by laser-emission. *Science* 231:486–488.
6. Ilchenko VS, Savchenkov AA, Matsko AB, Maleki L (2001) Nonlinear optics and crystalline whispering gallery mode cavities. *Phys Rev Lett* 86:3168–3171.
7. Michler P, et al. (2000) A quantum dot single-photon turnstile device. *Science* 290:2282–2285.
8. Yamamoto Y, Tassone F, Cao H (2000) *Semiconductor cavity quantum electrodynamics* (Springer, New York).
9. McCall SL, Levi AFJ, Slusher RE, Pearton SJ, Logan RA (1992) Whispering-gallery mode microdisk lasers. *Appl Phys Lett* 60:289–291.
10. Suzuki S, Hatakeyama Y, Kokubun Y, Chu ST (2002) Precise control of wavelength channel spacing of microring resonator add-drop filter array. *J Lightwave Technol* 20:745–750.
11. Armani AM, Kulkarni RP, Fraser S, Flagan RC, Vahala KJ (2007) Label-free, single-molecule detection with optical microcavities. *Science* 317:783–787.
12. Chiasera A, et al. (2009) Spherical whispering-gallery-mode microresonators. *Laser Photonics Rev* 4:457–482.

13. Serpenguzel A, Arnold S, Griffel G (1995) Excitation of resonances of microshperes on an optical-fiber. *Opt Lett* 20:654–656.
14. Choi SJ, Djordjev K, Choi SJ, Dapkus PD (2003) Microdisk lasers vertically coupled to output waveguides. *Photon Technol Lett* 15:1330–1332.
15. Cai M, Painter O, Vahala KJ (2000) Observation of critical coupling in a fiber taper to a silica-microsphere whispering-gallery mode system. *Phys Rev Lett* 85:74–77.
16. Srinivasan K, Painter O (2007) Linear and nonlinear optical spectroscopy of a strongly coupled microdisk-quantum dot system. *Nature* 450:862–865.
17. Nöckel JU, Stone AD (1996) *Optical Processes in Microcavities*, eds RK Chang and AJ Campillo (World Scientific, Singapore), chap 11.
18. Levi AFJ, et al. (1993) Directional light coupling from microdisk lasers. *Appl Phys Lett* 62:561–563.
19. Nockel JU, Stone AD (1997) Ray and wave chaos in asymmetric resonant optical cavities. *Nature* 385:45–47.
20. Gmachl C, et al. (1998) High-power directional emission from microlasers with chaotic resonators. *Science* 280:1556–1564.
21. Chern GD, et al. (2003) Unidirectional lasing from InGaN multiple-quantum-well spiral-shaped micropillars. *Appl Phys Lett* 83:1710–1712.
22. Hentschel M, et al. (2009) Angular emission characteristics of quantum cascade spiral microlasers. *Opt Express* 17:10335–10343.
23. Nöckel JU, Stone AD, Chang RK (1994) Q spoiling and directionality in deformed ring cavities. *Opt Lett* 19:1693–1695.
24. Wiersig J, Hentschel M (2008) Combining directional light output and ultralow loss in deformed microdisks. *Phys Rev Lett* 100:033901.
25. Yan CL, et al. (2009) Directional emission and universal far-field behavior from semiconductor lasers with Limaçon-shaped microcavity. *Appl Phys Lett* 94:251101.
26. Wang QJ, et al. (2009) Directional emission deformed microcavity quantum cascade lasers. *New J Phys* 11:125018.
27. Song Q, et al. (2009) Chaotic microcavity laser with high quality factor and unidirectional output. *Phys Rev A* 80:041807.
28. Yi CH, Kim MW, Kim CM (2009) Lasing characteristics of a Limaçon-shaped microcavity laser. *Appl Phys Lett* 95:141107.
29. Unterhinninghofen J, Wiersig J, Hentschel M (2008) Goos-Hänchen shift and localization of optical modes in deformed microcavities. *Phys Rev E* 78:016201.
30. Luneburg RK (1964) *Mathematical Theory of Optics* (Univ of California Press, Berkeley), Chap 3, p 132.
31. Faist J, Capasso F, Sivco DL, Hutchinson AL, Cho AY (1994) Quantum cascade laser. *Science* 264:553–556.
32. Gmachl C, et al. (1997) Long-wavelength (9.5–11.5 μm) microdisk quantum-cascade lasers. *IEEE J Quantum Electron* 33:1567–1573.
33. Sirnivasan K, et al. (2005) Optical loss and lasing characteristics of high-quality-factor AlGaAs microdisk resonators with embedded quantum dots. *Appl Phys Lett* 86:151106.
34. Yu N, et al. (2008) Small-divergence semiconductor lasers by plasmonic collimation. *Nat Photonics* 2:564–570.
35. Smythe EJ, Dickey MD, Whitesides GM, Capasso F (2009) A technique to transfer metallic nanoscale patterns to small and non-planar surfaces. *ACS Nano* 3:59–65.
36. Boriskina SV, Benson TM, Sewell P, Nosich AI (2006) Q-factor and emission pattern control of the WG modes in notched microdisk resonators. *IEEE J Select Topics Quantum Electron* 12:52–58.
37. Dettmann CP, Morozov GV, Sieber M, Waalkens H (2009) Unidirectional emission from circular dielectric microresonators with a point scatterer. *Phys Rev A* 80:063813.
38. Wiersig J, et al. (2009) Direct observation of correlations between individual photon emission events of a microcavity laser. *Nature* 460:245–249.